REVEALING THE PROPERTIES OF DARK MATTER IN THE MERGING CLUSTER MACS J0025.4−1222[*]

Maruša Bradač[1,x], Steven W. Allen[2], Tommaso Treu[1,y], Harald Ebeling[3], Richard Massey[4], R. Glenn Morris[2], Anja von der Linden[2], Douglas Applegate[2],

Draft version June 4, 2008

ABSTRACT

We constrain the physical nature of dark matter using the newly identified massive merging galaxy cluster MACS J0025.4−1222. As was previously shown by the example of the Bullet Cluster (1E0657-56), such systems are ideal laboratories for detecting isolated dark matter, and distinguishing between cold dark matter (CDM) and other scenarios (e.g. self-interacting dark matter, alternative gravity theories). MACS J0025.4−1222 consists of two merging subclusters of similar richness at $z = 0.586$. We measure the distribution of X-ray emitting gas from Chandra X-ray data and find it to be clearly displaced from the distribution of galaxies. A strong (information from highly distorted arcs) and weak (using weakly distorted background galaxies) gravitational lensing analysis based on Hubble Space Telescope observations and Keck arc spectroscopy confirms that the subclusters have near-equal mass. The total mass distribution in each of the subclusters is clearly offset (at $> 4\sigma$ significance) from the peak of the hot X-ray emitting gas (the main baryonic component), but aligned with the distribution of galaxies. We measure the fractions of mass in hot gas ($0.09^{+0.07}_{-0.03}$) and stars ($0.010^{+0.007}_{-0.004}$), consistent with those of typical clusters, finding that dark matter is the dominant contributor to the gravitational field. Under the assumption that the subclusters experienced a head-on collision in the plane of the sky, we obtain an order-of-magnitude estimate of the dark matter self-interaction cross-section of $\sigma/m < 4\mathrm{cm}^2\mathrm{g}^{-1}$, re-affirming the results from the Bullet Cluster on the collisionless nature of dark matter.

Subject headings: cosmology: dark matter – gravitational lensing – galaxies:clusters:individual:MACS J0025.4−1222

## 1. INTRODUCTION

One of the most important quests in cosmology is to understand the formation and evolution of galaxies and galaxy clusters. While the standard paradigm of cold dark matter (CDM) within a $\Lambda$CDM cosmology works well overall, discrepancies between the predictions of this model and observations remain (such as the abundance of substructure in halos, and the shapes of dark matter profiles, especially in dwarf systems). These issues can be resolved in several ways, for example by invoking warm and/or self-interacting dark matter.

Mergers of galaxy clusters are excellent laboratories to test such ideas. Not only are cluster mergers the most energetic events since the Big Bang, but, as demonstrated by a recent study of the Bullet Cluster (1E0657−56; Clowe et al. 2004, Bradač et al. 2006, Clowe et al. 2006),

[*] Based on observations made with the NASA/ESA Hubble Space Telescope, obtained at the Space Telescope Science Institute, which is operated by the Association of Universities for Research in Astronomy, Inc., under NASA contract NAS 5-26555. These observations are associated with program # GO11100 and GO10703. This work is also based on observations collected at the W.M. Keck Observatory.
[1] Department of Physics, University of California, Santa Barbara, CA 93106, USA
[2] Kavli Institute for Particle Astrophysics and Cosmology, Stanford University, 382 Via Pueblo Mall, Stanford, CA 94305-4060, USA
[3] Institute for Astronomy, University of Hawaii, 2680 Woodlawn Drive, Honolulu, HI 96822, USA
[4] Institute for Astronomy, Royal Observatory Edinburgh, Blackford Hill, Edinburgh EH9 3HJ, UK
[x] Hubble Fellow
[y] Sloan Fellow, Packard Fellow
Electronic address: marusa@physics.ucsb.edu

they provide a unique avenue by which to probe the self-interaction cross-section of dark matter particles and test alternative gravity theories.

In clusters with recent major merger activity, the positions of the dark matter and main baryonic component (the X-ray emitting gas) can become temporarily separated. This occurs because the gas is collisional and experiences ram pressure, whereas galaxies and (presumably) dark matter are effectively collisionless. A merging direction perpendicular to the line-of-sight maximizes the apparent separation, allowing observers to independently study the main baryonic and dark matter components. In the example of the Bullet Cluster, Clowe et al. (2004), Bradač et al. (2006), and Clowe et al. (2006) used X-ray and gravitational lensing data to derive mass maps for both the baryonic and dark matter components, clearly showing the presence and dominance of dark matter. In agreement with the standard CDM paradigm, these observations indicate that dark matter has to be in a near-collisionless form, with a scattering cross-section $\sigma/m < 0.7\mathrm{cm}^2\mathrm{g}^{-1}$ (Randall et al. 2007).

A recent study of the merging cluster A520 by Mahdavi et al. (2007) rests less easily within this simple picture. For A520, Mahdavi et al. (2007) find a central mass peak that contains gas and dark matter but no significant galaxy concentration. These authors argue that such a configuration could occur if dark matter is collisional with a self-interaction cross-section of $3.8 \pm 1.1\mathrm{cm}^2\mathrm{g}^{-1}$, a result that is inconsistent with the Bullet Cluster limits. However, the statistical significance of the result for A520 is not high and the dynamics of the cluster are more complicated than 1E0657−56, with A520 appearing to be in the late stages of multiple, complex merger

events.

It has also been argued that the optical and X-ray observations of 1E0657−56 might be explained without standard CDM, by instead modifying the theory of gravity (and thus the effects of gravitational lensing). Models using the modified Newtonian Dynamics (MOND) theory (e.g. Milgrom 1983, Bekenstein 2004) have, however, so far achieved only limited success in reproducing the weak lensing observations (e.g. Angus et al. 2006, Brownstein & Moffat 2007) and are unable to explain the observed strong lensing. Moreover, the application of MOND models to galaxy clusters in general still requires the presence of large masses of invisible matter, which are typically argued to be a mixture of massive neutrinos and cold baryons (e.g. Angus et al. 2007).

Clearly, a satisfactory resolution to this debate requires further observations of massive, merging clusters; preferably those with simple, two-body configurations. Using deep, ground-based optical imaging and short, snapshot Chandra exposures of clusters in the all-sky, X-ray flux-limited MAssive Cluster Survey (MACS) (Ebeling et al. 2001, 2007), we have identified the X-ray brightest, most massive, obvious post-merging clusters in the redshift range $0.3 < z < 0.7$. From this search, MACS J0025.4−1222 emerges as a massive, merging cluster with an apparently simple geometry, consisting of two large subclusters of similar richness, both at redshift $z = 0.586$, colliding in approximately the plane of the sky.

Owing to their high masses and favorable redshifts, MACS clusters are ideally suited to gravitational lensing studies. Here we use new, multi-color Hubble Space Telescope (HST) data to determine a projected mass map for MACS J0025.4−1222, using both strong and weak lensing information. When combined with the Chandra data, this allows us to map the distributions of dark matter, hot X-ray emitting gas, and stars. The dark matter is resolved into two main clumps, centered on the galaxy populations. The Chandra data reveal a single, clear X-ray peak located between the two optical/lensing subclusters. The observed offset between the locations of the hot gas and galaxies/lensing mass is in good agreement with the expectations for standard collisionless cold dark matter. Both 1E0657−56 and MACS J0025.4−1222 provide direct evidence for the existence of dark matter and can be used to estimate the self-interaction cross-section.

This paper is structured as follows. Section 2 describes the optical and X-ray data and reduction procedures. Section 3 discusses the dynamics of the cluster, based on optical spectroscopy. Section 4 presents the strong and weak gravitational lensing analysis and the mass reconstruction based on these data. Section 5 discusses the X-ray data analysis. Section 6 details the results on the stellar and X-ray gas mass fractions. In Section 7 we present our main result on the relative distributions of dark and baryonic matter in the cluster, and determine rough limits on the dark matter self-interaction cross-section. Our conclusions are summarized in Section 8.

Throughout the paper we assume a ΛCDM cosmology with $\Omega_{\mathrm{m}} = 0.3$, $\Omega_{\Lambda} = 0.7$, and Hubble constant $H_0 = 70 \ \mathrm{km \, s^{-1} \, Mpc^{-1}}$. At a redshift $z = 0.586$, the length scale is 6.61 kpc/arcsec.

## 2. OBSERVATIONS OF MACS J0025.4−1222

We observed MACS J0025.4−1222 with HST/ACS for 4140s in the F555W filter and 4200s in F814W (6 exposures each) as part of the Cycle 13 proposal GO-10703 (PI Ebeling, November 5 2006). We also obtained a 11000s F450W HST/WFPC2 observation (11 exposures) as a part of the Cycle 16 proposal GO-11100 (PI Bradač, June 9 2007). As a part of the MACS survey, the cluster has been observed in the BVRIz' bands with Subaru Suprime-Cam. Here we use ACS F814W as our primary weak lensing band because it has the largest number of resolved background sources for which shapes can be measured, and a well understood point spread function (PSF) (Rhodes et al. 2007). The other bands are used to aid the color matching for identifying strongly lensed systems and to exclude foreground objects from the weak lensing catalogs.

The demands placed by the lensing analysis require special care when reducing the images. The ACS images were reduced using the HAGGLES pipeline (P. Marshall et al. 2008, in preparation). A similar procedure was also followed for the WFPC2 data. The data reduction procedure is described in Bradač et al. (2007).

A sample of more than 200 objects in MACS J0025.4−1222 were targeted in the course of a DEIMOS/KECK spectroscopic campaign for the MACS survey (Ebeling et al. 2007). The DEIMOS data were reduced using the same procedure as described in Ma et al. (2008). In addition, LRIS/KECK (Oke et al. 1995) has been used to target likely multiply-imaged sources selected based on their colors in the HST data. One slitmask was used with an exposure of 6.3ks on September 13 2007. The LRIS data were reduced using a dedicated pipeline, developed and kindly made available by M. Auger (see also Auger et al. 2008).

MACS J0025.4−1222 has been observed twice with the Chandra X-ray Observatory, in November 2002 for 19.3 ksec (obsid 3251); and in August 2004 for 24.8 ksec (obsid 5010). Both observations were made with ACIS-I in VFAINT mode. We have analysed the data using version 3.4 of the CIAO software and CALDB version 3.3.0.1. Applying conservative filtering, we obtain clean exposures of 15.7 and 21.3 ksec for obsid 3251 and 5010, respectively (total 37 ksec). These two exposures were combined for imaging purposes, but fitted separately and simultaneously in the spectral analysis.

## 3. OPTICAL DYNAMICAL ANALYSIS

Using the redshifts obtained with DEIMOS, we measure the cluster redshift $z_{\mathrm{Cl}}$ and velocity dispersion $\sigma_{\mathrm{Cl}}$. This is done via an iterative algorithm to determine $z_{\mathrm{Cl}}$ and $\sigma_{\mathrm{Cl}}$ from galaxies within 1.5 Mpc from the peak of the X-ray emission (§5), and within $\pm 3\sigma_{\mathrm{Cl}}$ from $z_{\mathrm{Cl}}$. Both $z_{\mathrm{Cl}}$ and $\sigma_{\mathrm{Cl}}$ are calculated using the biweight estimator of Beers et al. (1990). Galaxies are allowed to re-enter the sample at each iteration. This yields $z_{\mathrm{Cl}} = 0.5857$ and $\sigma_{\mathrm{Cl}} = 835^{+58}_{-59} \ \mathrm{km \, s^{-1}}$, measured from 108 galaxies. The overall appearance of the redshift distribution is roughly Gaussian, with little evidence for a bimodal distribution (Fig. 1).

As a test for the presence of dynamical substructure, we compute the statistics suggested by Dressler & Shectman (1988). Briefly, this method measures local deviations from the overall cluster redshift and velocity dispersion, and compares the result to Monte Carlo realizations
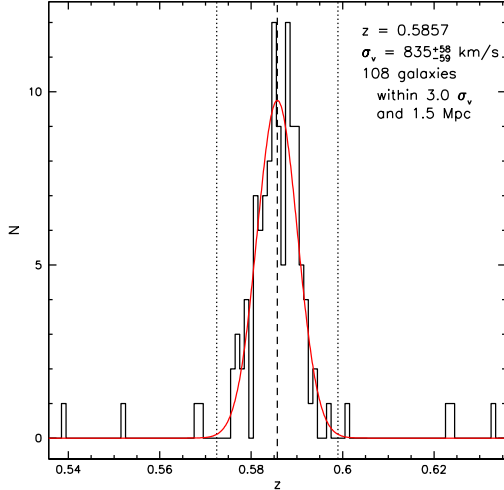
FIG. 1.— Histogram of the redshift distribution around the cluster redshift. Only galaxies within projected 1.5 Mpc are shown. The dashed line indicates the cluster redshift, the dotted lines the $\pm 3\sigma_{\rm Cl}$ limits used to calculate the cluster redshift and velocity dispersion. The Gaussian curve overplotted in red illustrates the measured velocity dispersion.

of the redshift and position values, where the redshifts have been randomized. The probability of finding larger deviations in the randomized cluster realizations is 3%, i.e. cluster substructure is marginally detected. This is mainly driven by some of the galaxies in the north-western subcluster, which have slightly lower than systemic redshifts.

The south-eastern (SE) subcluster has two equally-dominant galaxies (BCG1 and BCG2; their magnitudes are equal within the errorbars; see Fig. 3) of redshifts $z = 0.5856 \pm 0.0003$ and $z = 0.5838 \pm 0.0003$. The north-western (NW) one has a single dominant galaxy (BCG3) at a redshift $z = 0.5842 \pm 0.0003$. Assuming that the dominant galaxies lie at or near the minimima of the subcluster potentials, and averaging the redshifts of BCG1 and BCG2 in the SE subcluster, we infer a redshift difference between the NW and SE clumps of $\Delta z = 0.0005 \pm 0.0004$. This implies a line of sight velocity difference between the subclusters of $100 \pm 80 \, {\rm km \, s^{-1}}$. Given that the subclusters have collided, they have likely decoupled from the Hubble flow.

Based on this result and the measured velocity dispersion, we can obtain a crude estimate of the merger velocity and the angle of the merger axis relative to the plane of the sky. For 1E0657−56, Barrena et al. (2002) measure a velocity dispersion of $1132^{+117}_{-106} \, {\rm km/s}$ (from 52 early-type galaxy spectra) and Markevitch et al. (2006) estimate a merger velocity for 1E0657−56 (based on a 500ks Chandra observation) of $\sim 4500 \, {\rm km/s}$ (although this value is thought to be extreme; e.g. Hayashi & White 2006, Springel & Farrar 2007). Scaling by the ratio of these velocity dispersions, and assuming that the merger velocity in MACS J0025.4−1222 is more typical for a cluster of its mass, we crudely estimate a merger velocity of $\sim 2000 \, {\rm km \, s^{-1}}$. Given this merger velocity, the strong evidence that the subclusters in MACS J0025.4−1222 have merged recently, and the small, observed line-of-sight velocity difference between the subclusters, the

merger event is likely to have occured in close to the plane of the sky (within 5 degrees). The separation between the subclusters implies that closest approach occured a few $10^8$ years ago. Deeper X-ray data are required to refine our understanding of the geometry of the cluster.

## 4. LENSING ANALYSIS

The optical imaging data were used to identify multiply imaged sources (for strong lensing) and measure the distortion of background galaxies (for weak lensing). We then simultaneously fit these two data sets to obtain the (total) mass distribution of MACS J0025.4−1222.

### 4.1. Strong lensing features

Using the F450W/F555W/F814W HST and BVRIz' Subaru data, we have searched for multiply-imaged, lensed background sources. The positions of the multiple images used in the analysis are listed in Table 1 and shown in Fig. 3.
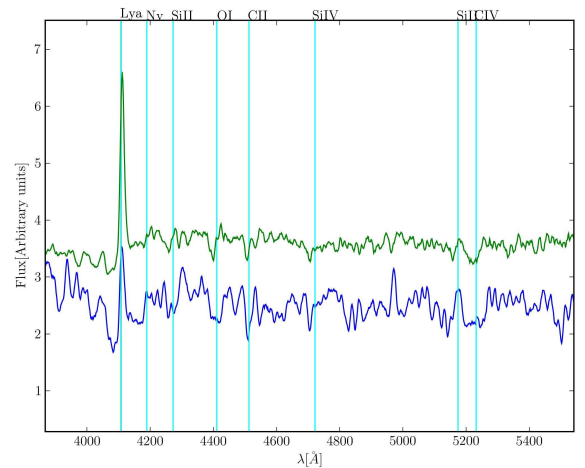


FIG. 2.— LRIS spectrum of the images A and B (a single slit was placed over both images). Lines redshifted to $z = 2.38$ are marked. Over-plotted (and offset for clariy) in green (top) is the composite Ly-break galaxy spectrum from Shapley et al. (2003). The emission line is significantly detected ($6\sigma$), no other significant features are seen in the spectrum.

We measure a spectroscopic redshift for system AB from the LRIS/KECK data of $z = 2.38$. This source has two distinct components (as seen from Fig. 3; hence the name AB) and we placed slits over both components each time. The spectrum of the northern of the three images is shown in Fig. 2, together with a composite Ly-break galaxy template from Shapley et al. (2003). A Ly-$\alpha$ emission line is significantly detected ($6\sigma$). The other two images had lower S/N spectra, but yield consistent results. For system C, we obtain a photometric redshift $z_{\rm C} = 1.0^{+0.5}_{-0.2}$ using the IRAF `polyphot` task and the HyperZ package (Bolzonella et al. 2000); this redshift is robust (i.e. there is no other likely redshift solution) due to the presence of the 4000Å break seen between the F555W and F814W bands. We have placed a slit over the northern of the two images and we see a tentative absorbtion feature at 7140Å. If interpreted as Mg II at 2799Å this gives a redshift of 1.55. However, the absorbtion feature is detected at a very low significance and no

other features are seen. Therefore we do not consider this identification as reliable and adopt the photometric redshift as our best estimate. Adopting the tentative spectroscopic redshift instead would not change our results significantly.

The photometric redshift of system D is less well determined. In addition the spectra did not have high enough S/N to obtain any spectroscopic redshift information. Using the photometric information we estimate $z_D = 2.8^{+0.4}_{-1.8}$.

The scarcity of reliably defined multiply imaged systems and spectroscopic redshifts limits our ability to determine an absolute calibration for the lensing mass map, due to the mass-sheet degeneracy (i.e. the reconstruction suffers from a degeneracy of the form $\kappa \to \kappa' = \lambda\kappa + (1 - \lambda)$, where $\lambda$ is an arbitrary constant, see e.g. Bradač et al. 2004a). This degeneracy can, in principle, be lifted when information from at least two source-redshift planes is available (see e.g. Seitz & Schneider 1997; since $\kappa$ is redshift-dependent, data from two redshifts can simultaneously constrain $\kappa$ and $\lambda$). In our case, we have only one spectroscopically-determined source redshift (around the NW peak). In principle, weak lensing data can provide a second effective redshift plane, allowing us to tightly constrain the mass, at least around the NW peak; in practice, however, the weak lensing data are too noisy to completely break the mass-sheet degeneracy (see e.g. Bradač et al. 2004b, Limousin et al. 2007). We might also, in principle, constrain the redshifts of systems C and D around the SE peak using the predictive power of the lens model. This requires the adoption of a specific family of models; which includes assumptions that lift the mass-sheet degeneracy, such as assuming zero mass at large distances. Moreover the constraints in regions far from the systems of known redshift tend to be weak.

### 4.2. *Weak lensing data*

Our weak lensing analysis of the HST/ACS data uses the RRG (Rhodes et al. 2000) galaxy shape measurement method, and the pipeline developed for the HST COSMOS survey (Massey et al. 2007). This has been tested and calibrated on simulated images containing a known weak lensing signal by Leauthaud et al. (2007). The MACS J0025.4−1222 and COSMOS observations use the same filter and are contemporary, although the COSMOS survey covered a much larger area of sky and provides a better calibration of instrumental systematics, including the camera's point spread function (PSF) and Charge Transfer Inefficiency (CTI). Thermal variations within HST's orbit cause it to expand and contract by a few microns (Rhodes et al. 2007). By matching the shapes of stars in the MACS J0025.4−1222 images to those in COSMOS fields (which were in turn compared to TinyTim models of the PSF, see Fruchter & Hook 2002), we determined that the focal length of HST (the distance between its primary and secondary mirrors) was $2\mu m$ shorter than nominal at the time of ACS exposure. This is a typical value (Leauthaud et al. 2007). We created a model of the PSF over the field of view and over all possible focus positions by interpolating the shapes of stars in all images within the COSMOS survey. Similarly, the PSF-corrected ellipticities of galaxies in the MACS J0025.4−1222 data were corrected for CTI trail-

TABLE 1
THE PROPERTIES OF THE
MULTIPLY-IMAGED SYSTEMS.

|   | RA | Dec | $z$ |
|---|---|---|---|
| A | 6.365628 | -12.36976 | |
|   | 6.363495 | -12.37609 | 2.38 |
|   | 6.363393 | -12.37276 | |
| B | 6.365353 | -12.36974 | |
|   | 6.363261 | -12.37606 | 2.38 |
|   | 6.363169 | -12.37268 | |
| C | 6.392082 | -12.38603 | |
|   | 6.391968 | -12.38757 | $1.0^{+0.5}_{-0.2}$ |
| D | 6.382898 | -12.38511 | |
|   | 6.384163 | -12.38253 | $2.8^{+0.4}_{-1.8}$ |
|   | 6.382926 | -12.38472 | |

NOTE. — The redshift of systems A and B were obtained using KECK spectroscopy (a single slit was placed over both components each time), whereas the others have been determined photometrically.

ing (associated with radiation damage in the ACS detectors) by subtracting the spurious ellipticity induced by this effect. This spurious ellipticity was modelled from the observed shapes of galaxies within the COSMOS survey as a function of object flux and position on the detectors (Rhodes et al. 2007).

From the final catalog we selected background objects, excluding cluster members using color information from the HST (F450W/F555W/F814W) images and spectroscopic data. Galaxies in the cluster red sequence are identified by two color criteria: $0.0 < m_{F555W} - m_{F450W} < 1.4$ and $1.8 < m_{F555W} - m_{F814W} < 3.0$. We furthermore exclude objects brighter in F814W than the three BCGs. We note that these cuts will not remove blue cluster members (and some bluer or redder foregrounds), which will dilute the weak lensing signal. However since the signal is mainly driven by the strong lensing data (see also Bradač et al. 2007) this will not bias our results significantly. Following Bradač et al. (2007), where data of similar depth were used, we assume the average redshift for galaxies in the weak lensing catalog to be $z_{WL} = 1.4$. Again the exact value has little influence on the end results (as discussed in §4.4) because it does not change the location of the peaks and only marginally affects the overall scaling of the surface mass density.

### 4.3. *Mass reconstruction of MACS J0025.4−1222*

Our combined strong and weak lensing analysis follows the method described in Bradač et al. (2005) and implemented on ACS data in Bradač et al. (2006, 2007). We describe the cluster's projected gravitational potential by a set of values on a regular grid $\psi_k$, from which all observable quantities are evaluated by finite differencing. For example, the scaled surface mass density $\kappa$ is related to $\psi$ via the Poisson equation, $2\kappa = \nabla^2\psi$ (where the physical surface mass density is $\Sigma = \kappa\,\Sigma_{crit}$ and $\Sigma_{crit}$ is a constant that depends upon the angular diameter distances between the observer, the lens, and the source). Similarly, the shear $\gamma = \gamma_1 + i\gamma_2$ and the deflection angle $\vec{\alpha}$ are derivatives of the potential $\gamma_1 = 0.5(\psi_{,11} - \psi_{,22})$, $\gamma_2 = \psi_{,12}$, and $\vec{\alpha} = \nabla\psi$. The advantage of such an approach is that we avoid strong assumptions regarding the
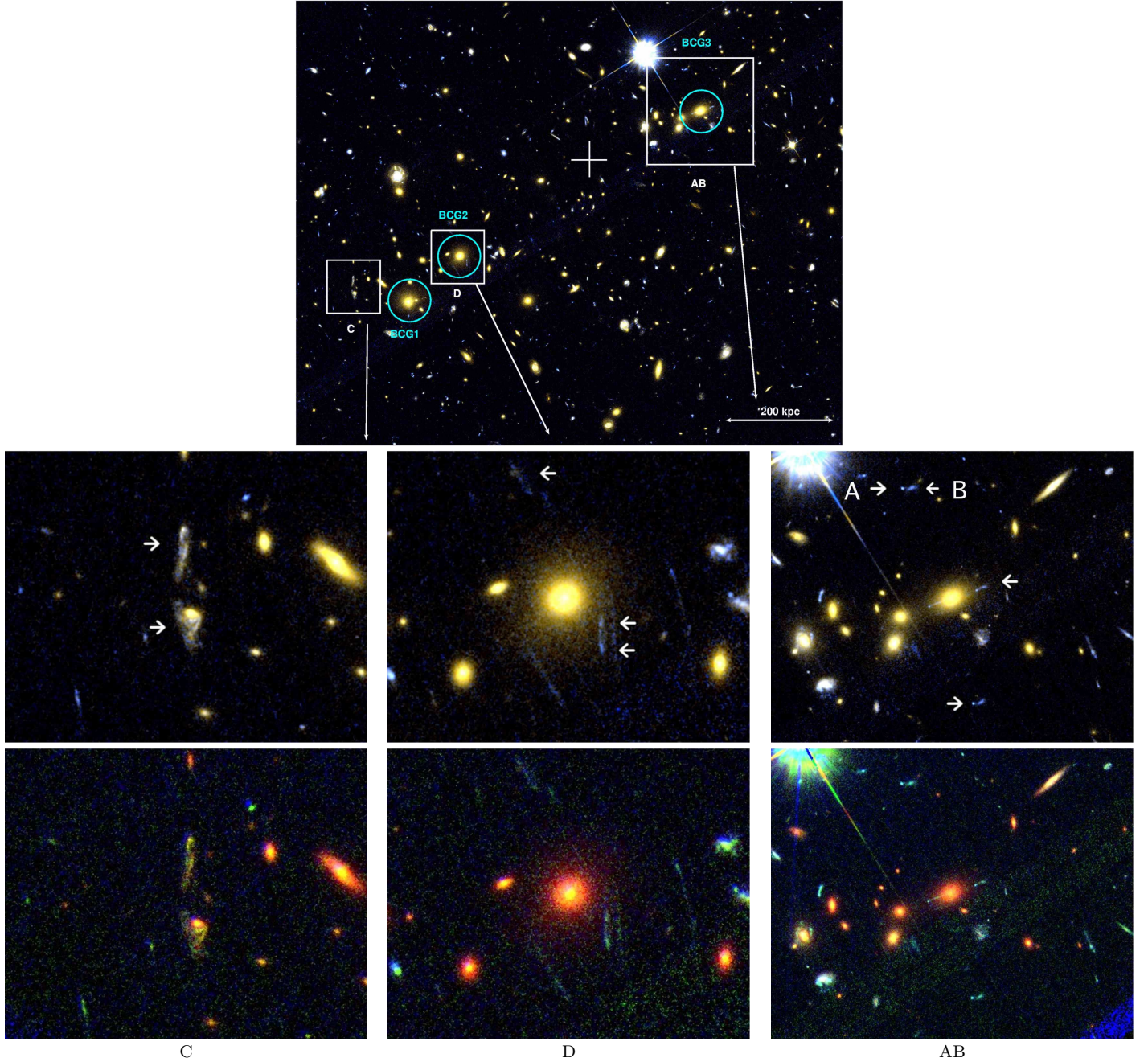
FIG. 3.— (top) The F555W-F814W color composite of the cluster MACS J0025.4−1222. North is up and East is left. The field is $2.5' \times 2.0'$. $15'' \times 15''$ cutouts (indicated in top panel) of C and D and $30'' \times 30''$ of the multiply imaged systems AB from the F555W-F814W (middle row) and F450W-F555W-F814W (bottom row) color composite are also shown. The three BCGs are marked with circles, the gas peak position with a + (with its size indicating the measured uncertainty, see §5).

shape and profile of the potential, which is crucial when dealing with merging clusters.

The strong and weak lensing data are combined in a $\chi^2$-fashion, minimizing the $\chi^2$ difference between the data and the model by searching for a solution to the non-linear equation $\partial\chi^2/\partial\psi_k = 0$. Hence we solve it in an iterative fashion (keeping the non-linear terms fixed at each iteration step). This requires an initial guess for the gravitational potential; the systematic effects arising from these particular choices are discussed below.

Figure 4 shows our best-fit reconstruction of the surface mass density, starting from an initial model consist-ing of two isothermal spheres, each of $\sigma = 1000\,\mathrm{km\,s^{-1}}$. The first sphere was centered between the two bright-est galaxies in the SE cluster (BCG1 and BCG2), and the second on the BCG of the NW subcluster (BCG3, see also Fig. 3). We also examined models in which the initial velocity dispersion of the spheres was reduced to $\sigma = 700\,\mathrm{km\,s^{-1}}$, and where the initial guess had zero mass: the resulting reconstruction did not change signif-icantly. Throughout the paper we will quote the results with the initial model using $\sigma = 1000\,\mathrm{km\,s^{-1}}$ as this model gives the best fit to the data. The other final solutions (encountered due to secondary minima in $\chi^2$

function) were however not significantly different.

The recovered distribution of mass in MACS J0025.4−1222 shows two distinct peaks, each centered approximately at the centers of the light distributions (galaxies). The measured positions and error bars are given in Table 2. The quoted error bars reflect the effects of exploring different initial conditions and other systematic effects (like misidentification of multiply imaged systems), and the statistical and systematic errors in the weak lensing data (see below). Table 3 lists the projected masses within 300 kpc of each of the BCG1 and BCG3, and the mass within 500 kpc of the X-ray peak.

### 4.4. *Systematic and statistical uncertainties*

As in previous work, we pay special attention to possible systematic effects when obtaining the surface mass density map. We have performed the following tests of robustness:

- **Initial Conditions:** Instead of assuming a two component mass model, we have examined the effects of starting with an "ignorant" model, i.e. assuming zero mass for the system. The final reconstructed peak positions differ little from those shown in Figure 4 and are well within the quoted error bars. We obtained a better fit, however, when using two isothermal spheres as initial conditions, hence the quoted numbers are from this reconstruction.

- **Multiply imaged system identification and redshifts:** Misidentification of multiply imaged systems can, in principle, significantly change the outcome of a reconstruction. We have examined the effects of removing one system at a time, as well as removing them all. While the absolute calibration of the mass distribution changes, the peak positions are not significantly altered and these changes are added in quadrature to the quoted error bars.

- **Statistical errors on weak lensing measurements:** The observed ellipticities of galaxies provide a noisy estimate of the local reduced shear $g = \gamma/(1-\kappa)$. We bootstrap resample the measured ellipticities to estimate the uncertainties. These are added to the errors discussed above to obtain the final estimate of the uncertainty on the measured positions and masses of the two peaks.

- **Systematic error budget on weak lensing measurements:** We estimate a $\sim 6\%$ uncertainty in the overall normalisation of the shear measurements. There is an additional $\sim 15\%$ calibration uncertainty from the assumption on the average redshift for galaxies in the final catalog. These uncertainties only affect the mass measurement (for which the systematic errors mentioned above dominate) and do not add to the positional uncertainty.

### 5. X-RAY DATA ANALYSIS

Using the Chandra data, we have constructed an exposure-corrected, 0.5−7.0keV, 4 arcsec/pixel count image of the central 4x4 arcmin region of the cluster. Two

TABLE 2
OFFSETS (WITH $1\sigma$ ERRORBARS) OF THE MASS PEAKS AND GAS PEAKS.

|  |  | $\Delta x$([arcmin]) | $\Delta y$([arcmin]) |
|---|---|---|---|
| SE | total | $-0.70 \pm 0.25$ | $-0.43 \pm 0.06$ |
|  | gas | $0.0 \pm 0.08$ | $0.0 \pm 0.08$ |
|  | galaxies | $-0.79 \pm 0.20$ | $-0.50 \pm 0.20$ |
| NW | total | $0.46 \pm 0.13$ | $0.20 \pm 0.04$ |
|  | gas | $0.0 \pm 0.08$ | $0.0 \pm 0.08$ |
|  | galaxies | $0.39 \pm 0.20$ | $0.18 \pm 0.20$ |

NOTE. — Offsets are calculated from (00:25:29.5, -12:22:36.6) which corresponds to the peak in gas distribution (marked with a white + in Fig. 3).

TABLE 3
*2-D projected* ENCLOSED MASS WITHIN A RADIUS OF 300kPC CENTERED ON BCG1 AND BCG3 AND WITHIN 500kPC CENTERED ON THE GAS PEAK.

|  |  | $M$ [$10^{14} M_\odot$] |
|---|---|---|
| SE - BCG1 | total | $2.5^{+1.0}_{-1.7}$ |
|  | galaxies | $0.027 \pm 0.008$ |
| NW - BCG3 | total | $2.6^{+0.5}_{-1.4}$ |
|  | galaxies | $0.019 \pm 0.006$ |
| Gas peak | total | $6.2^{+1.2}_{-4.0}$ |
|  | gas | $0.55 \pm 0.06$ |
|  | galaxies | $0.05 \pm 0.01$ |

NOTE. — Total projected masses are calculated from strong and weak lensing reconstruction, gas mass from Chandra X-ray data, and stellar mass from F814W data.

point sources in this region were removed, and the CIAO `dmfilth` tool used to fill in the excised regions by sampling from the distribution of surrounding pixels. The image was then adaptively smoothed using the `csmooth` tool, applying a sliding Gaussian kernel. The linearly-spaced contours derived from this image are shown in yellow in Fig. 4. The peak position in the adaptively smoothed X-ray contours is 00:25:29.5, -12:22:36.6. Although the precise position of this peak depends in detail on the smoothing algorithm, we conservatively estimate the accuracy to be better than 5 arcsec (i.e., the X-ray brightness peak is constrained to lie within 5 arcsec of this position). Significant X-ray emission from the cluster is detected out to a radius $\sim 150$ arcsec (1 Mpc).

The overall X-ray morphology of MACS J0025.4−1222 exhibits characteristics typical of a large merger event: the cluster shows a modest central surface brightness, high overall ellipticity and clear shifting of the X-ray centroid as a function of radius. Fitting a King model to the X-ray surface brightness profile, we measure a large core radius of $\sim 60$ arcsec (400kpc) which is also typical for large, merging clusters (e.g. Allen 1998).

We have carried out a spectral analysis of the Chandra data using the XSPEC code (version 11.3.2; Arnaud 1996). Background spectra were extracted from appropriate source-free regions of the ACIS-I chips. The Galactic absorption was fixed at the value of $2.5 \times 10^{20}$ cm$^{-2}$ derived from HI surveys (Kalberla et al. 2005). We use the MEKAL plasma emission code (Kaastra & Mewe 1993; incorporating the Fe-L calculations of
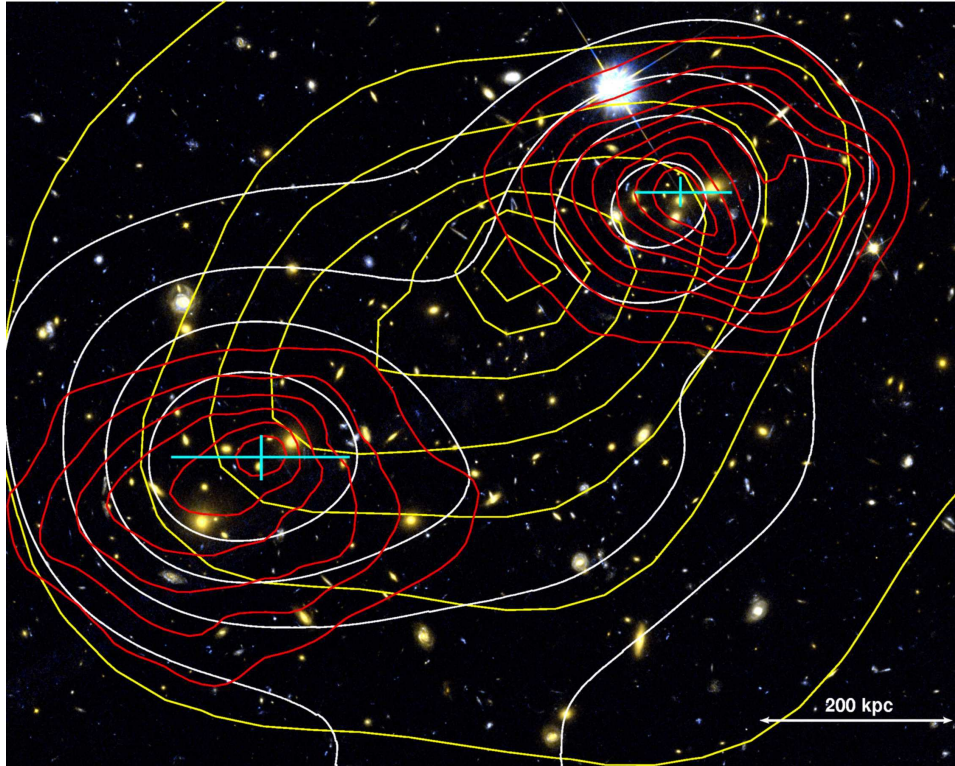
FIG. 4.— The F555W-F814W color composite of the cluster MACS J0025.4−1222. North is up and East is left. The field is $2.5' \times 2.0'$, which corresponds to $1000 \times 800$ kpc$^2$ at the redshift of the cluster. Overlaid in *red contours* is the surface mass density $\kappa$ from the combined weak and strong lensing mass reconstruction. The contour levels are linearly spaced with $\Delta\kappa = 0.1$, starting at $\kappa = 0.5$, for a fiducial source at a redshift of $z_{\rm s} \to \infty$. The X-ray brightness contours (also linearly spaced) are overlaid in *yellow* and the I-band light is overlaid in *white*. The measured peak position and errorbars for the total mass are given as a cyan cross (see Tab. 2).
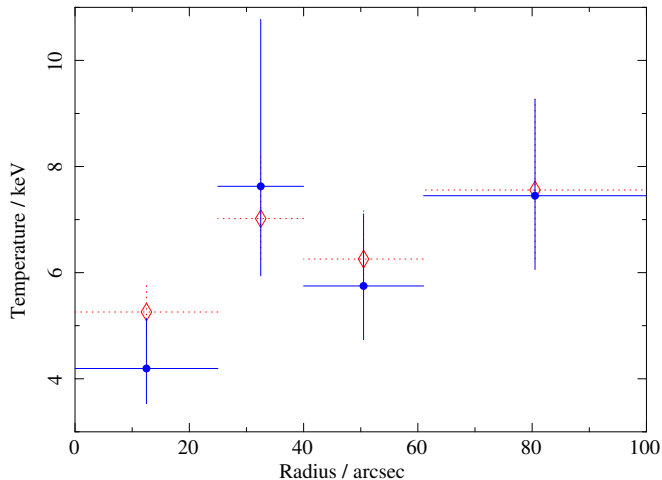


FIG. 5.— Temperature profiles of the X-ray gas. Red diamonds show the projected values, blue circles the deprojected values (assuming spherical symmetry and using a `projct` model to account for geometric effects). Error bars are $1\sigma$.
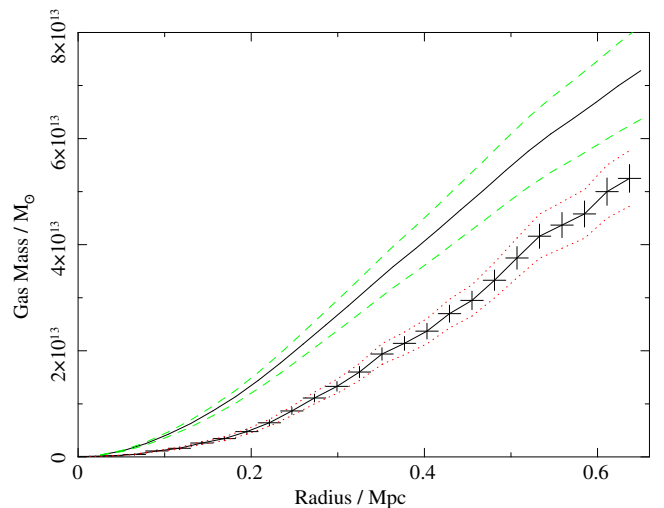


FIG. 6.— Mass profiles of the X-ray gas. The lower curve shows the mass within a sphere, the upper curve the projected mass within a cylinder along the line of sight, assuming the cluster extends to 1.5Mpc. The crosses show the statistical $1\sigma$ errors associated with each point, as obtained from the method of Allen et al. (2008). The red dotted lines show a (conservative) 10% systematic error (e.g.Nagai et al. 2007). The green dashed lines combine in quadrature the effect of a 10% systematic error on the projected mass with the effect of varying the outermost cluster radius from 1.1 to 2.0Mpc.

Liedahl et al. 1995) and the photoelectric absorption models of Balucinska-Church & McCammon (1992). The abundances of the elements were assumed to vary with a common ratio, $Z$, with respect to Solar values (Anders & Grevesse 1989). Only data in the 0.6–7.0 keV energy range were used.

Examining a circular region of radius 100 arcsec (660 kpc) centered on the X-ray peak, we measure a temper-

ature of $6.26^{+0.50}_{-0.41}$ keV and a metallicity $Z = 0.37 \pm 0.10$ solar. This spectrum contains approximately 4300 net (background-subtracted) counts. Dividing this region

into four annuli with approximately equal net counts, we obtain the (projected and deprojected) temperature profiles shown in Fig. 5. The deprojected metallicity rises from a value of 0.2 solar in the outer regions to > 1.0 within the central 25 arscec (∼ 160 kpc).

## 6. THE GAS AND STELLAR MASS CONTENT

The gas mass profile has been determined, under the assumption of spherical symmetry, using the deprojection method described by Allen et al. (2008). As discussed by e.g. Nagai et al. (2007), such an approach should provide an accurate measure of the gas mass, with systematic errors of < 10%, even for clusters experiencing major merger events. The deprojected gas mass profile, with statistical and (conservative) systematic error bars, is shown as the lower curve in Fig. 6. Within a spherical radius of 500 kpc, we measure a gas mass of $3.6 \pm 0.4 \times 10^{13}$ M$_\odot$. The *projected* gas mass within a cylinder along the line of sight is shown in the upper curve; this result is (slightly) sensitive to the outermost extent assumed for the cluster. The surface brightness profile is measurable out to 1.1Mpc, whereas a virial radius for a cluster of this temperature and redshift is expected to be ∼ 1.5Mpc. We therefore consider values from 1.1–2Mpc for the outermost cluster radius. Within the region plotted (for which X-ray temperature data are available), the variation in projected mass due to our choice of outer radius is less than 10% at all radii. The error-range displayed in Fig. 6 is formed from the sum in quadrature of this uncertainty and a conservative 10% systematic error. At 500kpc we measure a projected mass $(5.5 \pm 0.6) \times 10^{13}$ M$_\odot$.

We adopt the following procedure to measure the stellar mass distribution from the HST data. We identify cluster members based on color-color diagrams, with the color cuts described in §4.2, making use of the DEIMOS/KECK spectroscopic redshifts when available. These cuts primarily select red cluster members, which should be the dominant contributors to the total luminosity. To calculate the stellar mass, we transform observed $I$-band magnitudes (MAGAUTO, Bertin & Arnouts 1996) to K-band rest-frame luminosities, adopting an absolute solar magnitude $M_{\mathrm{K},\odot} = 3.28$, Galactic extinction following Schlegel et al. (1998) and Cardelli et al. (1989) with $A_{\mathrm{I}} = 0.054$, and K-correcting (we assume zero evolutionary correction) using an SED template for an elliptical galaxy from Coleman et al. (1980) (extended in the UV and IR regions with the GISSEL spectra, Bruzual A. & Charlot 1993). The resulting K-correction is 2.464.

We note that our template is likely slightly redder than the cluster members (possibly giving a larger stellar mass), although the approximation is adequate for our purposes. The resulting luminosity distribution (smoothed with a Gaussian kernel with FWHM 80 kpc) is shown in Fig. 4. To convert luminosities to stellar masses we follow Drory et al. (2004) and assume the stellar-mass-to-light ratio in K-band to be $M_*/L_{\mathrm{K}} = 0.74 \pm 0.30$ (see also Bell et al. 2003).

The enclosed, projected total mass within 500 kpc of the X-ray peak, and the projected masses in X-ray emitting gas and stars (in galaxies) are listed in Table 3. The gas mass fraction of $9^{+7}_{-3}\%$ is consistent with the typical value of ∼ 11% observed at similar radii in other

massive, X-ray luminous clusters (e.g.Allen et al. 2008; note that the value of 11% does not refer to the projected values, but the projection will make little difference given the errorbars). The mass-to-light ratio $(M/L_{\mathrm{K}}(< 500\mathrm{kpc}) = 130^{+40}_{-80})$ and stellar mass fraction $(1.0^{0.7}_{0.4}\%)$ within this aperture are also normal (see e.g. Kneib et al. 2003, Lin & Mohr 2004). Studying the inner regions of the two subclusters, we measure mass-to-light ratios of $M/L_{\mathrm{K}}(< 300\mathrm{kpc}) = 70^{+40}_{-50}$ and $100^{+40}_{-60}$ for the SE and NW peaks respectively, which are also consistent with values found for other clusters (see e.g. Kneib et al. 2003). Both subclusters have a stellar-to-total mass ratio of 1 per cent within 300 kpc.

## 7. DISSECTING MACS J0025.4−1222 INTO DARK MATTER AND BARYONS

Figure 4 shows the distributions of galaxies, X-ray emitting gas and total mass in MACS J0025.4−1222. The figure clearly demonstrates our main result: an obvious spatial offset is observed between the peak of the X-ray emission and the twin peaks of the total mass distribution. As in the case of 1E0657−56, we see a good alignment between the total mass and light distribution. The offsets between the X-ray and total mass components are significant at > 4σ for both the SE and NW clumps (see Table 2). We calculate the significance by assuming that the errors on the total mass distribution follow Gaussian distribution and those on the peak gas position a top-hat function. This is conservative, since both strong and weak lensing (separately) give the peak positions within the observed multiple images, hence the lensing errors are also unlikely to be Gaussian.

Like the Bullet Cluster, the morphology and properties of MACS J0025.4−1222 are consistent with those of a high velocity merger event approximately in the plane of the sky. Given a sound speed for the X-ray emitting gas of ∼ 1300 km s$^{-1}$ and a collision velocity of order 2000 km s$^{-1}$, the merger is likely to have been supersonic; clearly it was violent enough to have separated the baryonic and dark matter cores. The existing, short Chandra exposures are insufficient to indentify and measure shock fronts in the cluster; a deeper Chandra observation of MACS J0025.4−1222 is required. Such a Chandra observation would also permit detailed thermodynamic mapping of the cluster (e.g. Million & Allen 2008).

In contrast to 1E0657−56, neither of the subclusters in MACS J0025.4−1222 contains an X-ray bright, relatively cool, dense 'bullet' of low-entropy gas. This is not suprising; at low-to-intermediate redshifts only a fraction (tens of per cent) of clusters contain such cores (e.g. Peres et al. 1998, Bauer et al. 2005). Once formed, these cores are expected to be relatively robust and, after the merger event, eventually settle at the base of the newly-formed cluster potential. Thus, whereas in 1−2 Gyr time MACS J0025.4−1222 may still not possess a cool core, 1E0657−56 appears likely to evolve into a cool-core cluster.

### 7.1. *Limits on self-interaction cross-section and dark matter alternatives*

Following Markevitch et al. (2004) and based on the new data for MACS J0025.4−1222, we can make

an order-of-magnitude estimate for the self-interaction cross-section of dark matter. In the first case, the observed offset between the gas and total mass component implies that the scattering depth of dark matter particles $\tau = \Sigma\sigma/m$ during the collision cannot be much greater than 1. The surface mass density $\Sigma$ at the position of both peaks averaged over a radius of 150kpc is $\sim (0.25 \pm 0.10)$g cm$^{-2}$. Assuming that the two subclusters experienced a head-on collision within this radius, we obtain an estimate for the scattering cross-section of $\sigma/m < 4$cm$^2$g$^{-1}$. The assumption of spherical symmetry (we assume that the surface mass density along the collision direction is similar to that along the line-of-sight) appears reasonable in MACS J0025.4−1222 with both subclusters showing little ellipticity.

Secondly, the apparent survival of the dark matter content after the recent merger event, implied by the mass-to-light ratios, confirms that the dark matter needs to be collisionless (Markevitch et al. 2004). Unfortunately current constraints on the escape velocity and shock velocity are too weak to derive more stringent limits on the cross-section. Better X-ray data, improved lensing constraints and detailed hydrodynamical simulations are required to significantly improve upon on these constraints.

Just like 1E0657−56, MACS J0025.4−1222 severely challenges modified gravities theories such a MOND (e.g. Milgrom 1983) and TeVeS (Bekenstein 2004). Angus et al. (2006) attempt to explain the weak lensing data for 1E0657−56 using a MOND-like model with 2 eV neutrinos. However, such neutrinos alone cannot explain the X-ray properties of groups (Angus et al. 2007), and lie at the limit of the allowed region from current neutrino experiments (Maintz/Troitsk; e.g. Weinheimer 2003). Moreover, such as model cannot easily explain the tight strong lensing constraints on the mass distributions in the inner regions of 1E0657−56 and MACS J0025.4−1222, where multiple images are observed.

## 8. CONCLUSIONS AND OUTLOOK

We have presented new data for the post-merging galaxy cluster MACS J0025.4−1222. This system exhibits many similar properties to the Bullet Cluster 1E0657−56, although it does not contain a low-entropy, high density hydrodynamical 'bullet'. HST and Chandra data have allowed us to derive a high-resolution total mass map, as well as the X-ray gas mass and stellar mass distributions in the cluster. Our main conclusions are as follows:

1. The total mass distribution in MACS J0025.4−1222 shows two distinct peaks. Both are clearly offset from the main baryonic component (the hot gas) as traced by the X-ray emission, at $> 4\sigma$ significance (for each of the peaks). There is no significant offset between the peaks of the total mass distribution and the galaxies.

2. We have measured the projected, enclosed mass of the three main mass constituents (dark matter, gas, and stars) within 500 kpc of the X-ray center. The gas-to-total mass ratio ($9^{+7}_{-3}\%$) and the mass-

to-light ratio ($1.0^{+0.7}_{-0.4}\%$) are typical for a massive cluster.

3. The mass-to-light ratios $M/L_{\mathrm{K}}$ ($< 300$kpc) $= 70^{+40}_{-50}$ and $100^{+40}_{-60}$ for the SE and NW peak, and the stellar-to-total mass ratios ($1.0^{+0.7}_{-0.4}\%$) in these regions are consistent with values for other massive clusters, arguing that there was no significant loss of dark matter from either subcluster during the collision.

4. The majority of the mass is spatially coincident with the galaxies which implies, just as for the Bullet Cluster, that the cluster must be dominated by a relatively collisionless form of dark matter. We obtain an estimate for the self-interaction cross-section $\sigma/m < 4$cm$^2$g$^{-1}$.

MACS J0025.4−1222 is a remarkable cluster with properties that allow us to improve our understanding of the details of cluster formation and evolution, and the nature of dark matter. Our results can be further improved with additional strong lensing information to better constrain the normalization of the mass model and better X-ray data to improve the determination of the merger speed, and hence improve the limits on the dark matter cross-section. Discovering more clusters like MACS J0025.4−1222 and 1E0657−56 will also improve the systematic uncertainties on dark matter self-interaction cross-section inherent to the study of a small number of these objects.

REFERENCES

Allen, S. W. 1998, MNRAS, 296, 392

Allen, S. W., Rapetti, D. A., Schmidt, R. W., Ebeling, H., Morris, R. G., & Fabian, A. C. 2008, MNRAS, 383, 879

Anders, E. & Grevesse, N. 1989, Geochim. Cosmochim. Acta, 53, 197

Angus, G. W., Famaey, B., & Buote, D. A. 2007, ArXiv:0709.0108, 709

Angus, G. W., Famaey, B., & Zhao, H. S. 2006, MNRAS, 371, 138

Arnaud, K. A. 1996, in Astronomical Society of the Pacific Conference Series, Vol. 101, Astronomical Data Analysis Software and Systems V, ed. G. H. Jacoby & J. Barnes, 17–+

Auger, M. W., Becker, R. H., & Fassnacht, C. D. 2008, AJ, 135, 1311

Balucinska-Church, M. & McCammon, D. 1992, ApJ, 400, 699

Barrena, R., Biviano, A., Ramella, M., Falco, E. E., & Seitz, S. 2002, A&A, 386, 816

Bauer, F. E., Fabian, A. C., Sanders, J. S., Allen, S. W., & Johnstone, R. M. 2005, MNRAS, 359, 1481

Beers, T. C., Flynn, K., & Gebhardt, K. 1990, AJ, 100, 32

Bekenstein, J. D. 2004, Phys. Rev. D, 70, 083509

Bell, E. F., McIntosh, D. H., Katz, N., & Weinberg, M. D. 2003, ApJS, 149, 289

Bertin, E. & Arnouts, S. 1996, A&AS, 117, 393

Bolzonella, M., Miralles, J.-M., & Pelló, R. 2000, A&A, 363, 476

Bradač, M., Clowe, D., Gonzalez, A., Marshall, P., Forman, W., Jones, C., Markevitch, M., Randall, S., Schrabback, T., & Zaritsky, D. 2006, ApJ, 652, 937

Bradač, M., Lombardi, M., & Schneider, P. 2004a, A&A, 424, 13

Bradač, M., Schneider, P., Lombardi, M., & Erben, T. 2005, A&A, 437, 39

Bradač, M., Schneider, P., Lombardi, M., Steinmetz, M., Koopmans, L. V. E., & Navarro, J. F. 2004b, A&A, 423, 797

Bradač, M., Schrabback, T., Erben, T., McCourt, M., Million, E., Mantz, A., Allen, S., Blandford, R., Halkola, A., Hildebrand, H., Lombardi, M., Marshall, P., Schneider, P., Treu, T., & Kneib, J.-P. 2007, ArXiv:0711.4850, 711

Brownstein, J. R. & Moffat, J. W. 2007, MNRAS, 382, 29

Bruzual A., G. & Charlot, S. 1993, ApJ, 405, 538

Cardelli, J. A., Clayton, G. C., & Mathis, J. S. 1989, ApJ, 345, 245

Clowe, D., Bradač, M., Gonzalez, A. H., Markevitch, M., Randall, S. W., Jones, C., & Zaritsky, D. 2006, ApJ, 648, L109

Clowe, D., Gonzalez, A., & Markevitch, M. 2004, ApJ, 604, 596

Coleman, G. D., Wu, C.-C., & Weedman, D. W. 1980, ApJS, 43, 393

Dressler, A. & Shectman, S. A. 1988, AJ, 95, 985

Drory, N., Bender, R., Feulner, G., Hopp, U., Maraston, C., Snigula, J., & Hill, G. J. 2004, ApJ, 608, 742

Ebeling, H., Barrett, E., Donovan, D., Ma, C.-J., Edge, A. C., & van Speybroeck, L. 2007, ApJ, 661, L33

Ebeling, H., Edge, A. C., & Henry, J. P. 2001, ApJ, 553, 668

Fruchter, A. S. & Hook, R. N. 2002, PASP, 114, 144

Hayashi, E. & White, S. D. M. 2006, MNRAS, 370, L38

Kaastra, J. S. & Mewe, R. 1993, Legacy, 3, 16

Kalberla, P. M. W., Burton, W. B., Hartmann, D., Arnal, E. M., Bajaja, E., Morras, R., & Pöppel, W. G. L. 2005, A&A, 440, 775

Kneib, J., Hudelot, P., Ellis, R. S., Treu, T., Smith, G. P., Marshall, P., Czoske, O., Smail, I., & Natarajan, P. 2003, ApJ, 598, 804

Leauthaud, A., Massey, R., Kneib, J.-P., Rhodes, J., Johnston, D. E., Capak, P., Heymans, C., Ellis, R. S., Koekemoer, A. M., Le Fèvre, O., Mellier, Y., Réfrégier, A., Robin, A. C., Scoville, N., Tasca, L., Taylor, J. E., & Van Waerbeke, L. 2007, ApJS, 172, 219

Liedahl, D. A., Osterheld, A. L., & Goldstein, W. H. 1995, ApJ, 438, L115

Limousin, M., Richard, J., Jullo, E., Kneib, J.-P., Fort, B., Soucail, G., Elíasdóttir, Á., Natarajan, P., Ellis, R. S., Smail, I., Czoske, O., Smith, G. P., Hudelot, P., Bardeau, S., Ebeling, H., Egami, E., & Knudsen, K. K. 2007, ApJ, 668, 643

Lin, Y.-T. & Mohr, J. J. 2004, ApJ, 617, 879

Ma, C.-J., Ebeling, H., Donovan, D., & Barrett, E. 2008, ArXiv e-prints, 805

Mahdavi, A., Hoekstra, H., Babul, A., Balam, D. D., & Capak, P. L. 2007, ApJ, 668, 806

Markevitch, M., Gonzalez, A. H., Clowe, D., Vikhlinin, A., Forman, W., Jones, C., Murray, S., & Tucker, W. 2004, ApJ, 606, 819

Markevitch, M., Randall, S., Clowe, D., Gonzalez, A., & Bradac, M. 2006, in COSPAR, Plenary Meeting, Vol. 36, 36th COSPAR Scientific Assembly, 2655–+

Massey, R., Rhodes, J., Ellis, R., Scoville, N., Leauthaud, A., Finoguenov, A., Capak, P., Bacon, D., Aussel, H., Kneib, J.-P., Koekemoer, A., McCracken, H., Mobasher, B., Pires, S., Refregier, A., Sasaki, S., Starck, J.-L., Taniguchi, Y., Taylor, A., & Taylor, J. 2007, Nature, 445, 286

Milgrom, M. 1983, ApJ, 270, 384

Million, E. & Allen, S. 2008, Submitted to MNRAS

Nagai, D., Vikhlinin, A., & Kravtsov, A. V. 2007, ApJ, 655, 98

Oke, J. B., Cohen, J. G., Carr, M., Cromer, J., Dingizian, A., Harris, F. H., Labrecque, S., Lucinio, R., Schaal, W., Epps, H., & Miller, J. 1995, PASP, 107, 375

Peres, C. B., Fabian, A. C., Edge, A. C., Allen, S. W., Johnstone, R. M., & White, D. A. 1998, MNRAS, 298, 416

Randall, S. W., Markevitch, M., Clowe, D., Gonzalez, A. H., & Bradač, M. 2007, ArXiv:0704.0261, 704

Rhodes, J., Refregier, A., & Groth, E. J. 2000, ApJ, 536, 79

Rhodes, J. D., Massey, R. J., Albert, J., Collins, N., Ellis, R. S., Heymans, C., Gardner, J. P., Kneib, J.-P., Koekemoer, A., Leauthaud, A., Mellier, Y., Refregier, A., Taylor, J. E., & Van Waerbeke, L. 2007, ApJS, 172, 203

Schlegel, D. J., Finkbeiner, D. P., & Davis, M. 1998, ApJ, 500, 525

Seitz, C. & Schneider, P. 1997, A&A, 318, 687

Shapley, A. E., Steidel, C. C., Pettini, M., & Adelberger, K. L. 2003, ApJ, 588, 65

Springel, V. & Farrar, G. R. 2007, MNRAS, 380, 911

Weinheimer, C. 2003, hep-ex/0306057